

INFLUENCE OF GRAIN SIZE AND SHAPE ON MECHANICAL PROPERTIES OF METAL AM MATERIALS

R. Saunders[†], A. Achuthan[‡], A. Iliopoulos[†], J. Michopoulos[†], and A. Bagchi[†]

[†]Materials Science and Technology Division, U.S. Naval Research Laboratory, Washington, DC,
20375

[‡]Dept. of Mechanical and Aeronautical Engineering, Clarkson University, Potsdam NY, 13676

Abstract

Metal powder-based additive manufacturing (PAM) typically results in microstructures with a texture and columnar grain structure. The columnar grains can vary greatly in size and shape throughout the microstructure, which can significantly affect the mechanical properties of the resulting part. A previous study developed a microstructurally informed crystal plasticity constitutive model that took into account grain sizes and shapes then showed that grain geometry can influence the prediction of mechanical behavior of the part. In the present work, the influence of grain aspect ratio, size, and loading direction on the resulting mechanical properties of the PAM part are investigated through a parametric study. Results show that considering size and shape effects have the tendency to increase the material yield strength while decreasing the initial strain hardening modulus. Using this knowledge, it may be possible to optimize a PAM microstructure using process parameters to produce a part which exhibit superior yield strength and hardening moduli compared to traditional materials.

Introduction

Metal powder-based additive manufacturing (PAM) processes involve continued melting and solidification of metallic powder. The rate at which material cools after solidification as determined by the thermal gradient, influences the evolution of the local microstructure. Large thermal gradients lead to substantial local stresses in the solidified material [1]. Because of the elevated temperature, the yield stress of the material is substantially decreased meaning that the local thermal stress can lead to local yielding of the material. Local yielding results in non-uniform plastic strain which, when coupled to the mechanical constraint of the support structure (e.g. the base plate), may cause large residual stress and undesirable distortion of the build part. Residual stresses in the build part have been suggested to deteriorate fatigue strength [2] and decrease PAM part's service life. Additionally, the stress evolution in the microstructure may produce defects, such as dislocations, pores, and microcracks [3].

The microstructure resulting from a PAM process typically has a texture due to epitaxial grain growth. The grains are often columnar with different grain sizes and aspect ratios, which affect the mechanical properties of the material. To numerically study these effects, a number of

This material is declared a work of the U.S. Government and is not subject to copyright protection
in the United States. Approved for public release; distribution is unlimited.

finite element (FE) models have been developed. Early models primarily focused on challenges associated with a moving heat source, material evolution, and computational cost of the simulation [4, 5, 6, 7, 8, 9]. Subsequent studies focused on residual stress evolution and the role of process parameters in the PAM process in influencing these residual stress [10, 11, 12, 13, 14, 15]. A more recent study [16] focused on the development of a microstructure-informed constitutive model developed to describe the mechanical behavior of solidified material produced by PAM by extending the recently reported [17, 18] microstructural-feature size-dependent crystal plasticity constitutive model for nickel superalloy materials. A follow-up study [19] developed a method to better capture the grain boundaries, and therefore grain shape, to more accurately represent the local stress intensification of irregularly shaped grains.

In this work, the models developed previously [16, 19, 20] are extended to examine the effects of grain size and shape on the prediction of the mechanical behavior of a material. First, an overview of the crystal plasticity model along with its implementation is presented. Next, synthetic microstructures that contain features seen in PAM microstructures are generated and meshed to create an FE model of a representative volume element (RVE). The generated FE models are used to conduct a parametric study where average RVE aspect ratio and grain size are varied. As part of this study, the constitutive response is varied to consider cases with no size or shape effects, size effects only, and both size and shape effects. The effect of load direction is also examined by considering longitudinal (i.e., along the dominant grain direction) and transverse (i.e., out of plane of the dominant grain direction) tension and shear.

Constitutive Model and Homogenization

The crystal plasticity constitutive model implemented in this work is an extension of the grain-size dependent crystal plasticity constitutive model described in [17, 18]. The constitutive model has been extended by [16] to account for the aspect ratio of grains and is based on a core and mantle framework to describe the effect of a grain boundary. In this framework, a grain boundary influence region where there is an increased resistance to dislocation nucleation is considered. The resistance to dislocation nucleation in the region has a maximum value at the grain boundary and fades away at the inner boundary of the region in the grain. The resistance in the grain boundary influence region is represented in a fashion similar to that of work-hardening, where the grain boundary effects are associated with an increase in strength and decrease in initial strain-hardening modulus. By treating the grain boundary influence similar to work-hardening, the crystal plasticity constitutive modeling framework used to capture work-hardening effects can be implemented. A brief overview of the framework is presented here to elucidate how the grain boundary effects are incorporated; further details can be found in [16].

The instantaneous shear strength of a slip system, α , at a material point at location r in the grain boundary influence region can be stated as the additive decomposition,

$$g^{(\alpha)}(r, t) = g_0^{(\alpha)} + g_{GB}^{(\alpha)}(r) + g_L^{(\alpha)}(r, t), \quad (1)$$

where $g_0^{(\alpha)}$ is the shear strength of the material points outside the grain boundary influence region

of an annealed sample, $g_{GB}^{(\alpha)}(r)$ represents the grain boundary effect on the strength, $g_L^{(\alpha)}(r, t)$ represents the increase in strength due to strain-hardening as a result of mechanical loading, and r and t are location and time, respectively. The resistance to dislocation motion due to the grain boundary effect has no evolution in time. Thus, it can be represented as an integration in the total strain in all slip systems, $d\gamma$, according to

$$g_{GB}^{(\alpha)}(r) = \int_0^{\tilde{\gamma}_{GB}(r)} \dot{g}^{(\alpha)}(\tilde{\gamma}, \dot{\gamma}^{(\beta)}) d\gamma, \quad (2)$$

where $\dot{g}^{(\alpha)}$ is the rate of strain hardening, β is any slip system, $\dot{\gamma}$ is the shear flow rate, and γ is the cumulative shear flow strain. The grain boundary effects and the effects from loading, as stated above, appear the same as a work hardening type behavior. However, the grain boundary effect is not a physical quantity but rather a mathematical one introduced to allow for a variation in strength and initial strain hardening modulus. As such, this quantity must be separated appropriately from the actual strain caused by loading and is denoted with the $(\tilde{})$ symbol. Equation 2 can be simplified by use of the strain-hardening modulus, $h_{\alpha\beta}$, so that

$$g_{GB}^{(\alpha)}(r) = \int_0^{\tilde{\gamma}_{GB}(r)} \Sigma_{(\beta)} h_{\alpha\beta}(\tilde{\gamma}) |\dot{\gamma}^{(\beta)}| d\gamma. \quad (3)$$

Equation 3 can be further simplified by considering the special case of a hyperbolic secant squared type strain-hardening with

$$h_{\alpha\beta} = q^{\alpha\beta} h_{0\infty} \operatorname{sech}^2 \left| \frac{h_{0\infty} \gamma}{\tau_s - \tau_{0\infty}} \right|, \quad (4)$$

where $q^{\alpha\beta}$ differentiates latent-hardening ($\alpha \neq \beta$) and self hardening ($\alpha = \beta$), $h_{0\infty}$ is the initial hardening modulus, and τ_s is the maximum resistance to shear flow. The previous equations are very general since they are defined on a material point basis. However, the computational implementation of the equations on a material point basis can be challenging for a realistic 3D microstructure. In this work, an alternative approach using homogenization on a grain-by-grain basis is utilized. The total strength can be rewritten as,

$$g^{(\alpha)}(r, t) = \tau_{0\infty} + \overline{g_{GB}} + \int_0^t \dot{g}^{(\alpha)} dt, \quad (5)$$

where

$$\overline{g_{GB}} = g_{GB}^{(\alpha)}(\overline{\tilde{\gamma}_{GB}}) \quad (6)$$

and

$$\overline{\tilde{\gamma}_{GB}} = \frac{\int_{V_{GB}} \tilde{\gamma}_{GB}(r) dV}{V}. \quad (7)$$

The above integration is aided by mapping the arbitrary grain geometry to a simplified domain, such as a sphere or an ellipsoid. Considering only size effects, a simple sphere with the volume equivalent of the grain is sufficient to represent the grain. The diameter of this sphere is found as $d = \sqrt[3]{\frac{3V}{\pi}}$, where d is the diameter of the representative sphere and V is the known grain volume of the arbitrarily shaped grain. Considering both the size and shape effects requires the use of an

ellipsoid, which can be represented by a general quadric surface $\psi(x, y, z) = 0$, where $\psi(x, y, z)$ is a quadratic polynomial given by,

$$\begin{aligned} \psi(x, y, z) = & A_1x^2 + A_2y^2 + A_3z^2 + \\ & A_4xy + A_5yz + A_6xz + \\ & A_7x + A_8y + A_9z + A_{10} \end{aligned} \quad (8)$$

Individual grains are then represented using an ellipsoid that provides the best fit in terms of minimum linear least square (llsq) error. The approach essentially uses all the known points on the arbitrary grain surface to determine the appropriate coefficients, A_i , for the given grain. With a known integrable grain geometry, the integration in Equation 7 can be performed by assuming a constant grain boundary thickness, δ_{GB} , and parameterizing the ellipsoid and grain boundary in terms of the radii.

Model Generation

In this work, RVEs of microstructures that are similar in nature to those identified experimentally via Electron Back Scattering Diffraction (EBSD) imaging in actual PAM microstructures are synthesized using a continuum diffuse interface model [20]. The resulting synthetic microstructure generated by the continuum diffuse interface model is represented in figure 1. The data in the RVE is in the form of a 3D matrix with each (i, j, k) location containing a grain label from 1 to N , where N is the total number of distinct grains in the microstructure. The structure of this data is similar to the data structure used in gray scale images such as those obtained from magnetic resonance imaging (MRI) and computed tomography (CT) scans. As such, the voxel image data is imported into ScanIP, a software developed by Simpleware (Synopsys, Mountain View, USA) to semi-automatically segment such image data.

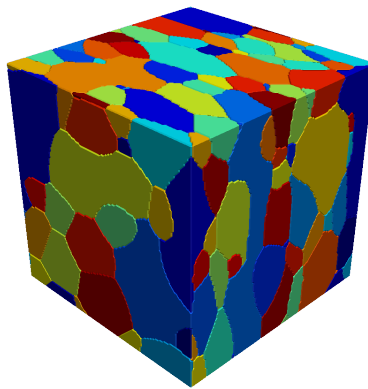


Figure 1: RVE of synthetic microstructure generated by the 3-D continuum diffuse interface model.

The segmentation process creates a surface representation of each grain, which is then used to generate a surface and volume FE mesh. To eliminate the “stair stepping” effect inherent to the data structure, an algorithm to anti-alias and smooth the data is applied to ensure smooth

contours along the grain boundaries. Following the smoothing of the surface data, the segmented boundaries are converted into a triangulated surface representation, then a multi-part surface decimation algorithm followed by a Delaunay tessellation with tetrahedral elements is applied [21]. A tetrahedral mesh is used in this work as it better represents the grain geometries (and therefore overall RVE behavior) at a similar or lower computational cost compared to a hexahedral mesh [19].

The finite element model in this work is implemented in Abaqus/Standard (Dassault Systems, Providence, RI, USA) implicit FEA package [22], with the crystal plasticity constitutive model highlighted earlier, implemented through a user material subroutine (UMAT). The RVE faces have periodic boundary conditions applied. The constitutive model parameters used in this work are taken from a copper cubic lattice structure and from literature [23, 24]. The copper cubic lattice structure used to define the elastic material properties C_{11} , C_{12} , and C_{44} and the plastic material parameters \dot{a} , n , and q were obtained from [23]. The parameters \dot{a} and n are the parameters for a power law flow rule. The material properties $\tau_{0\infty}$, τ_s and $h_{0\infty}$ (eq. 4) were determined by matching the stress-strain behavior of a grain-size independent simulation with the stress-strain behavior reported for the sample with large average grains [24]. A grain boundary thickness δ_{GB} of $0.333 \mu m$ was chosen. All the material parameters used in this study are shown in Table 1.

Table 1: Material parameters used for the numerical simulation.

Parameters	Value
$\tau_{0\infty}$	9 MPa
τ_s	95 MPa
\dot{a}	0.001 /s
n	10
q	1
C_{11}	168.4 GPa
C_{12}	121.4 GPa
C_{44}	75.4 GPa
$\tilde{\gamma}_{GB}^*$	1.07
$h_{0\infty}$	240 MPa

Note that the value of n obtained from the previously referenced works [23, 24] was 100, but a value of 10 is used in this study. The parameter n controls the rate dependence of the material and higher values of n result in a more intensive computational problem. To demonstrate the effect of the n variability, identical problems were run with only the value of n varying from 10 to 100 (Figure 2). Figure 2a shows how the choice of n influences the predicted stress-strain behavior and Figure 2b shows how n influences computational time. The stress-strain behavior is relatively unaffected except for the absolute value of the predicted stress. However, the computational time using $n = 10$ compared to using $n = 100$ is increased by a factor of 4. The goal of this study is to generate large amounts of comparative data, thus $n = 10$ was chosen to expedite the data col-

lection process. The results of the study are not affected by this choice as the material parameters are irrelevant as long as they are consistent between analyses. The results only show changes in predicted mechanical behavior due to changes in how the grains in the RVE are represented, i.e. no size or shape effect, size effect (grains represented by a sphere), or size and shape effect (grains represented by an ellipsoid). The trends seen between runs due to changing grain size/aspect ratio and load direction are being analyzed in this purely computational study.

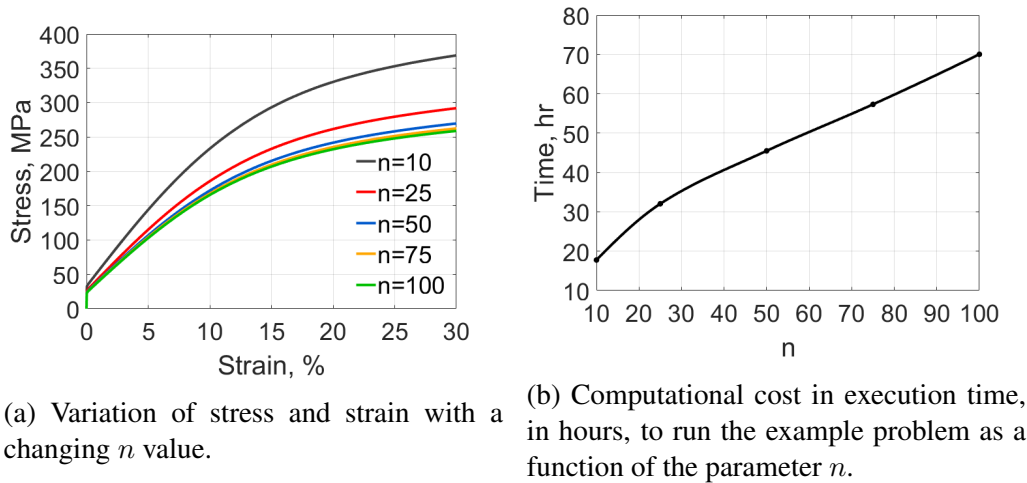


Figure 2: The effect of varying n on mechanical behavior prediction and computational time.

Results and Discussion

Three RVE microstructures are generated and analyzed in the parametric study presently being conducted. The three RVEs are generated by using three different combinations of parameters in the continuum diffuse interface model. The RVEs are referred to by the anisotropy factor κ_0 that controls the anisotropy associated with the grain aspect ratios as described in [20]. Three κ_0 values of 1, 3, and 5.5 were chosen to generate RVEs with three distinctly different aspect ratios as shown by Figure 3. The three κ_0 values were chosen to simulate an equiaxial grain structure ($\kappa_0 = 1$) such as that seen in the traditional manufacturing process, a slightly directionally-biased grain structure ($\kappa_0 = 3$), and a highly elongated grain structure ($\kappa_0 = 5.5$). The last two are representative of features that can be seen in PAM microstructures. Each RVE has approximately 300 grains and a volume of 0.1 mm^3 .

The variation of grain size and shape throughout each of the RVEs is shown in Figure 4, where the grain effective diameter is calculated by equating the grain volume to a sphere and the effective aspect ratio is the largest axis of the fitted ellipsoid to the mean of the intermediate and smallest axes. From Figure 4a, it can be seen that the number of grains and effective diameter of the grains in each microstructure are approximately the same. This indicates that the three RVEs contain similar number of grains with similar volumes, thus the largest variability in the RVEs are the shapes of the grains. The effective aspect ratios of Figure 4b show the expected behavior that as

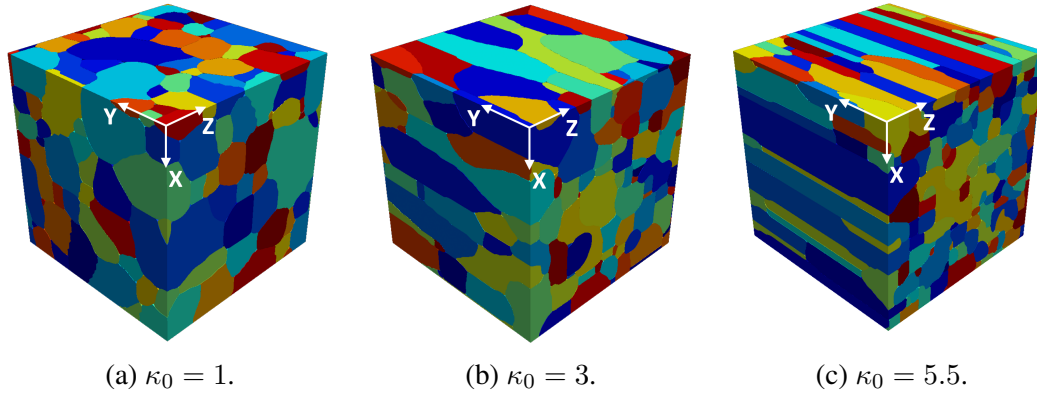
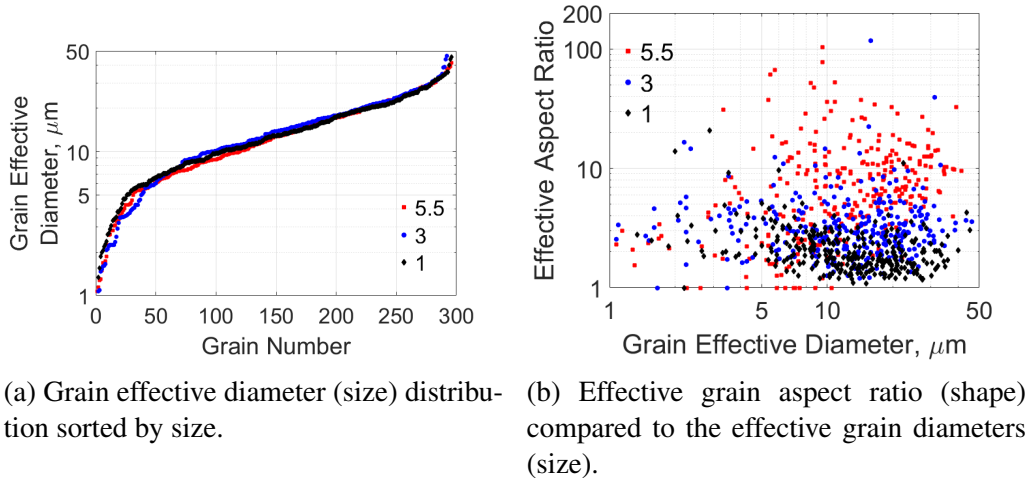


Figure 3: Synthetic microstructure RVEs generated by the continuum diffuse interface model with three different values of κ_0 .

κ_0 is increased the variability in the aspect ratio is increased. However, the increase in κ_0 does not mean that grains with a low aspect ratio are completely removed, the inverse is also true. This is easily demonstrated by noting that the highest effective aspect ratio of the three RVEs is actually in the $\kappa_0 = 3$ case and not the $\kappa_0 = 5.5$ case, but on average the effective aspect ratio in the $\kappa_0 = 5.5$ case is higher than the $\kappa_0 = 3$ case.



(a) Grain effective diameter (size) distribution sorted by size.

(b) Effective grain aspect ratio (shape) compared to the effective grain diameters (size).

Figure 4: Synthetic microstructure RVE grain size and shape distributions.

The generated RVEs are now used in the previously described parametric study. The goal of this study is to determine how the grain boundary effect changes the stress-strain behavior of the three synthetic RVEs under four different loading conditions. The RVEs are subjected to a uniaxial tensile loading in the dominant grain direction (Y direction in figure 3) and a direction transverse to this direction (Z direction in figure 3). An in-plane ($Y - Z$ direction in figure 3) and an out-of-plane ($X - Z$ direction in figure 3) shear loading were also considered. Here we have assumed that loading in the X and Z directions and shear in the $X - Y$ and $Y - Z$ planes produces identical behavior. The loading is applied via a specified displacement to generate a

maximum volume-averaged nominal strain in the direction of the load of 60%. The analysis results were post-processed by volume averaging the stress and strain in the direction of the load. Other components of stress and strain not in the direction of the applied displacement were nonzero to maintain equilibrium but are not considered here. The cumulative results of the parametric study are shown in Figure 5. Note that these results include data up to 30% strain, as after that point all results have reached the saturation stress, thus coincided with one another and do not contribute to the discussion.

The first observation that can be noted is that by not including size and/or aspect ratio (AR) effects, the yield point for all values of κ_0 is unchanged for the different loading directions, as expected. Furthermore, the yield point for similar loading (e.g., tension or shear) when not considering size and/or shape effects is also unchanged. Intuitively, this is an unexpected behavior because it is well known that materials with a dominant material orientation such as those seen in PAM-produced parts, generally have an anisotropic response (e.g., carbon fiber-epoxy composites and biological materials such as muscle). This reinforces the need for a constitutive model that incorporates grain size and shape effects. Next, these results show that in tension an increasing RVE aspect ratio (controlled by κ_0) has the effect of decreasing the stress at 30% strain but in shear, has the effect of increasing the stress at this point. This effect is independent of the grain boundary effect. Including the size effect increases the yield strength and decreases the strain hardening modulus. This effect is amplified when considering the size and shape effects and further amplified when the microstructure average AR is increased. Due to the RVE grain sizes being the same, on average, the size effect does not vary with varying κ_0 . Finally, it can be seen that in all cases, the yield point is heavily influenced by grain shape. However, the predicted hardening modulus for the elongated grains is lower than the more conventional microstructure.

It is difficult to draw quantitative conclusions on the effect that the grain boundary has on the stress-strain behavior. However, it can be said that the grain shape and size both have a discernible effect on the mechanical behavior of the PAM part. It is also known that grain size and shape are influenced by the process parameters involved in producing the PAM part. The combination of these facts leads to the conclusion that the process parameters can be directly related to the mechanical properties of the PAM produced part.

Conclusions

The work in the present paper has described an overview of the implementation of a constitutive model that incorporates grain size and shape effects. Synthetic microstructure representative volume elements were generated using a continuum diffuse interface model. RVEs of three different aspect ratios, representative of PAM microstructures, were generated and then converted to finite element meshes. The FE models were implemented in Abaqus/Standard with the crystal plasticity model implemented in a UMAT. The FE models of the RVEs were used to complete a parametric study to determine the effects of grain size and shape on effective mechanical properties of the RVE.

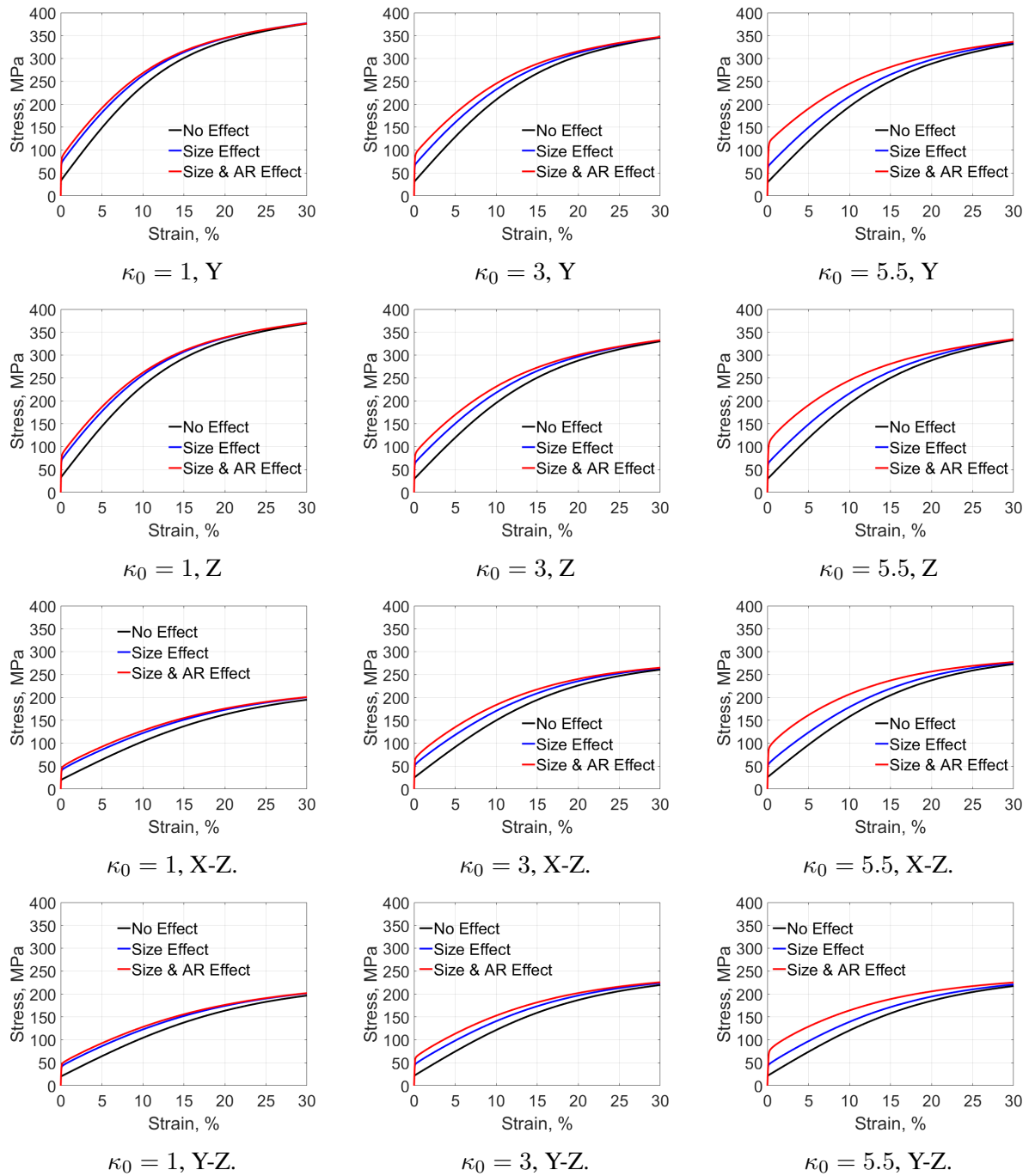


Figure 5: Results of the parametric study varying RVE anisotropy factor (κ_0), grain boundary effect applied, and load direction.

As part of the parametric study, three synthetic RVEs were simulated under four loading conditions with and without grain boundary effects applied. The results showed that when both the size and shape effects are considered, the loading in the direction of the elongated grains produced superior strength compared to the out-of-plane loading. Finally, it was concluded that the grain boundary effect had the most significant effect immediately post yield with the effect diminishing as the material strength reached the saturated strength.

With a known connection between process parameters and microstructure, it may be possible to utilize the framework and the insight gained from this work to optimize a microstructure so that it would exhibit superior yield strength while maintaining a higher hardening modulus compared to traditionally manufactured microstructures. The optimized structure could then be related back to specific PAM process parameters and the parts exhibiting the superior behavior could be built.

Acknowledgments

We acknowledge the Sabbatical Faculty Fellowship with the Technology Management Training Group, Inc. (TMT Group), and support by US Naval Research Laboratory and Clarkson University for AA. Partial support for this project was provided by the Office of Naval Research (ONR) through the Naval Research Laboratorys Basic Research Program. This work was supported in part by a grant of computer time from the DOD High Performance Computing Modernization Program at the Army Engineer Research and Development Center (ERDC) DoD Supercomputing Resource Centers (DSRC).

References

- [1] J.-P. Kruth, L. Froyen, J. Van Vaerenbergh, P. Mercelis, M. Rombouts, and B. Lauwers, "Selective laser melting of iron-based powder," Journal of Materials Processing Technology, vol. 149, no. 1, pp. 616–622, 2004.
- [2] G. Kasperovich and J. Hausmann, "Improvement of fatigue resistance and ductility of tial6v4 processed by selective laser melting," Journal of Materials Processing Technology, vol. 220, pp. 202 – 214, 2015.
- [3] R. Li, Y. Shi, Z. Wang, L. Wang, J. Liu, and W. Jiang, "Densification behavior of gas and water atomized 316l stainless steel powder during selective laser melting," Applied Surface Science, vol. 256, no. 13, pp. 4350 – 4356, 2010.
- [4] M. Matsumoto, M. Shiomi, K. Osakada, and F. Abe, "Finite element analysis of single layer forming on metallic powder bed in rapid prototyping by selective laser processing," International Journal of Machine Tools and Manufacture, 2002.

- [5] R. B. Patil and V. Yadava, "Finite element analysis of temperature distribution in single metallic powder layer during metal laser sintering," International Journal of Machine Tools and Manufacture, vol. 47, no. 7, pp. 1069–1080, 2007.
- [6] D. Zhang, Q. Cai, J. Liu, L. Zhang, and R. Li, "Select laser melting of w–ni–fe powders: simulation and experimental study," The International Journal of Advanced Manufacturing Technology, vol. 51, no. 5, pp. 649–658, 2010.
- [7] I. Roberts, C. Wang, R. Esterlein, M. Stanford, and D. Mynors, "A three-dimensional finite element analysis of the temperature field during laser melting of metal powders in additive layer manufacturing," International Journal of Machine Tools and Manufacture, vol. 49, no. 1213, pp. 916 – 923, 2009.
- [8] C. Fu and Y. Guo, "Three-dimensional temperature gradient mechanism in selective laser melting of ti-6al-4v," Journal of Manufacturing Science and Engineering, vol. 136, no. 6, p. 061004, 2014.
- [9] L.-E. Loh, C.-K. Chua, W.-Y. Yeong, J. Song, M. Mapar, S.-L. Sing, Z.-H. Liu, and D.-Q. Zhang, "Numerical investigation and an effective modelling on the selective laser melting (slm) process with aluminium alloy 6061," International Journal of Heat and Mass Transfer, vol. 80, pp. 288–300, 2015.
- [10] K. Dai and L. Shaw, "Distortion minimization of laser-processed components through control of laser scanning patterns," Rapid Prototyping Journal, vol. 8, no. 5, pp. 270–276, 2002.
- [11] A. Nickel, D. Barnett, and F. Prinz, "Thermal stresses and deposition patterns in layered manufacturing," Materials Science and Engineering: A, vol. 317, no. 1, pp. 59–64, 2001.
- [12] L. Ma and H. Bin, "Temperature and stress analysis and simulation in fractal scanning-based laser sintering," The International Journal of Advanced Manufacturing Technology, vol. 34, no. 9-10, pp. 898–903, 2007.
- [13] A. Hussein, L. Hao, C. Yan, and R. Everson, "Finite element simulation of the temperature and stress fields in single layers built without-support in selective laser melting," Materials and Design, vol. 52, no. 0, 2013.
- [14] L. Papadakis, A. Loizou, J. Risse, and J. Schrage, "Numerical computation of component shape distortion manufactured by selective laser melting," Procedia {CIRP}, vol. 18, pp. 90 – 95, 2014. Proceedings of the International Conference on Manufacturing of Lightweight Components - ManuLight 2014.
- [15] R. Paul, S. Anand, and F. Gerner, "Effect of thermal deformation on part errors in metal powder based additive manufacturing processes," Journal of Manufacturing Science and Engineering, vol. 136, no. 3, 2014.
- [16] A. Achuthan, A. Iliopoulos, J. Michopoulos, R. Saunders, and A. Bagchi, "Towards a constitutive model that encapsulates microstructural features induced by powder additive manufacturing," in ASME 2017 International Design Engineering Technical Conferences and

Computers and Information in Engineering Conference, American Society of Mechanical Engineers, 2017.

- [17] M. G. Moghaddam, A. Achuthan, B. A. Bednarczyk, S. M. Arnold, and E. J. Pineda, “Development of a precipitate size-dependent crystal plasticity constitutive model for two-phase materials and its implementation on a multi-scale computational framework,” Materials Science and Engineering: A, vol. 651, pp. 893 – 903, 2016.
- [18] M. Ghorbani Moghaddam, A. Achuthan, B. A. Bednarczyk, S. M. Arnold, and E. J. Pineda, “Grain size-dependent crystal plasticity constitutive model for polycrystal materials,” Materials Science and Engineering A, vol. 703, no. July, pp. 521–532, 2017.
- [19] R. Saunders, A. Bagchi, and A. Achuthan, “A method to determine local stress fields in microstructure features produced by additive manufacturing,” in ASME 2017 International Mechanical Engineering Congress and Exposition, pp. V002T02A025–V002T02A025, American Society of Mechanical Engineers, 2017.
- [20] J. G. Michopoulos, A. P. Iliopoulos, J. C. Steuben, A. J. Birnbaum, Y. Fu, and J.-H. Song, “Towards computational synthesis of microstructural crystalline morphologies for additive manufacturing applications,” in ASME 2017 International Design Engineering Technical Conferences and Computers and Information in Engineering Conference, pp. V001T02A030–V001T02A030, American Society of Mechanical Engineers, 2017.
- [21] P. G. Young, T. B. H. Beresford-West, S. R. L. Coward, B. Notarberardino, B. Walker, and A. Abdul-Aziz, “An efficient approach to converting three-dimensional image data into highly accurate computational models,” Philosophical Transactions of the Royal Society A: Mathematical, Physical and Engineering Sciences, vol. 366, no. 1878, pp. 3155–3173, 2008.
- [22] Dassault Systèmes Simulia Corp., “Abaqus 2017, Theory, Benchmarks, and Examples Manuals,” 2017.
- [23] Y. Huang, A user-material subroutine incorporating single crystal plasticity in the ABAQUS finite element program. 1991.
- [24] N. Hansen and B. Ralph, “The strain and grain size dependence of the flow stress of copper,” Acta Metallurgica, vol. 30, no. 2, pp. 411 – 417, 1982.